



1 A comparison between the GNSS tomography technique and the 2 WRF model in retrieving 3D wet refractivity field in Hong Kong

3 Zhaohui Xiong¹, Bao Zhang^{1*}, and Yibin Yao^{1*}

4 ¹ School of Geodesy and Geomatics, Wuhan University, Wuhan 430079;
5 cehui_xiong@whu.edu.cn (Z.X.); ybyao@whu.edu.cn (Y.Y.)

6 * Correspondence: Bao Zhang (sggzb@whu.edu.cn); Yibin Yao (ybyao@whu.edu.cn)

7 **Abstract.** Water vapor plays an important role in various scales of weather processes. However, there are
8 limited means to monitor its 3-dimensional (3D) dynamical changes. The Numerical Weather Prediction
9 (NWP) model and the Global Navigation Satellite System (GNSS) tomography technique are two of the
10 limited means. Here, we conduct an interesting comparison between the GNSS tomography technique and
11 the Weather Research and Forecasting (WRF) model (a representative of the NWP models) in retrieving Wet
12 Refractivity (WR) in Hong Kong area during a rainy period and a rainless period. The GNSS tomography
13 technique is used to retrieve WR from the GNSS slant wet delay. The WRF Data Assimilation (WRFDA)
14 model is used to assimilate GNSS Zenith Tropospheric Delay (ZTD) to improve the background data. The
15 WRF model is used to generate reanalysis data using the WRFDA output as the initial values. The radiosonde
16 data are used to validate the WR derived from the GNSS tomography and the reanalysis data. The Root Mean
17 Square (RMS) of the tomographic WR, the reanalysis WR that assimilate GNSS ZTD, and the reanalysis
18 WR that without assimilating GNSS ZTD are 6.50 mm/km, 4.31 mm/km and 4.15 mm/km in the rainy period.
19 The RMS becomes 7.02 mm/km, 7.26 mm/km and 6.35 mm/km in the rainless period. The lower accuracy
20 in the rainless period is mainly due to the sharp variation of WR in the vertical direction. The results also
21 show that assimilating GNSS ZTD into the WRFDA model only slightly improves the accuracy of the
22 reanalysis WR and that the reanalysis WR is better than the tomographic WR in most cases. However, in a
23 special experimental period when the water vapor is highly concentrated in the lower troposphere, the
24 tomographic WR outperforms the reanalysis WR in the lower troposphere. When we assimilate the
25 tomographic WR in the lower troposphere into the WRFDA model, the reanalysis WR is improved.

26 1. Introduction

27 Water vapor (WV), mostly contained in the troposphere, plays an important role in various scales of
28 atmospheric processes. But due to its active nature, there are limited models and techniques that can accurately
29 describe or monitor its 3-dimensional (3D) dynamical changes (Rocken et al., 1993).

30 The development of Global Navigation Satellite System (GNSS) technique and the densely deployed GNSS
31 receivers provide us the opportunity to monitor the WV field in near real time. When GNSS signal travels
32 through the neutral atmosphere, it undergoes time delay and bending due to the atmospheric refractivity. This
33 effect is usually called the tropospheric delay in the GNSS field (Altshuler, 2002). The tropospheric delay is
34 usually considered as the product of the zenith delay and the mapping function (Lanyi, 1984; Niell, 1996).
35 The Zenith Tropospheric Delay (ZTD) consists of two parts: the hydrostatic part and the wet part. The wet



36 delay is mainly associated with the WV and reflects WV content in the troposphere. Bevis et al. (Bevis et al.,
37 1992) introduced the principle of using GNSS Zenith Wet Delay (ZWD) to retrieve the Precipitable Water
38 Vapor (PWV). Since then, many scientists carried out the GNSS PWV experiments (Askne and Nordius, 1987;
39 Bokoye et al., 2003; Yao et al., 2014; Lu et al., 2015; Shoji and Sato, 2016). Now, the GNSS PWV can be
40 retrieved with an uncertainty of 1-2 mm in post-processing (Tregoning et al., 1998; Adams et al., 2011;
41 Grejner-Brzezinska, 2013) or real-time modes (Yuan et al., 2014; Li et al., 2014; Li et al., 2015).

42 The GNSS WV tomography technique was first proposed to monitor the 3D or 4D WV in 2000 (Flores et
43 al., 2000; Seko et al., 2000; Hirahara et al., 2000). Since then, many scientists have proposed refined methods
44 to improve the GNSS WV tomography (Flores et al., 2001; Nilsson and Gradinarsky, 2006; Rohm and Bosy,
45 2011; Wang et al., 2014; Wang et al., 2014; Zhao and Yao, 2017). The GNSS WV tomography methods can
46 be roughly categorized into two groups. One group solves the tomography equation in the least squares scheme
47 or in the Kalman filter scheme with additional constraints or using a priori information (Flores et al., 2000;
48 Rohm and Bosy, 2011; Cao et al., 2006; Zhang et al., 2017). The other group uses the algebraic reconstruction
49 algorithm or similar methods (Bender et al., 2011; Wang et al., 2014; Zhao and Yao, 2017). Some scientists
50 also use different methods from the above to solve the GNSS WR tomography (Nilsson and Gradinarsky,
51 2006; Perler et al., 2011; Altuntac, 2015). Though the tomography technique has the advantages of (1) free of
52 weather conditions and (2) retrieve 3D WR field in near real time, it still suffers some problems. The sparse
53 distribution of the GNSS receivers and the bad satellite-receiver geometry lead to serious ill-posed and ill-
54 conditioned problems, and also limit the WR retrieve resolution in both vertical and horizontal domains.

55 Besides the GNSS tomography technique, the WR can also be retrieved by numerical weather prediction
56 models (Gutman and Bock, 2007; Perler et al., 2011). The Weather Research and Forecasting (WRF) model
57 is a state-of-the-art atmospheric modeling system that is used to simulate the dynamic processes of the
58 atmosphere (Jankov et al., 2005; Carvalho et al., 2012). It is mainly developed and supported by
59 Mesoscale and Microscale Meteorology (MMM) Laboratory of the National Center for Atmospheric Research.
60 Many studies have demonstrated that assimilating ZTD/PWV into WRF can improve the reanalysis water
61 vapor field (Pacione et al., 2001; Faccani et al., 2005; Boniface et al., 2012; Bennitt and Jupp, 2012; Moeller
62 et al., 2016; Lindskog et al., 2017).

63 Both the GNSS tomography technique and the WRF model could retrieve 3D WR field. It will be
64 interesting to compare their capabilities in retrieving WR field under different weather conditions and to
65 explore the feasibility to combine them. For this purpose, we conduct GNSS tomography and data assimilation
66 experiments in Hong Kong area using the Hong Kong SatRef Network in a rainy period and a rainless period.
67 WR fields retrieved from GNSS tomography and WRF reanalysis are validated by the radiosonde data. We
68 also explore the feasibility of assimilating the GNSS tomographic WR into the WRF model to further improve
69 the WR field.

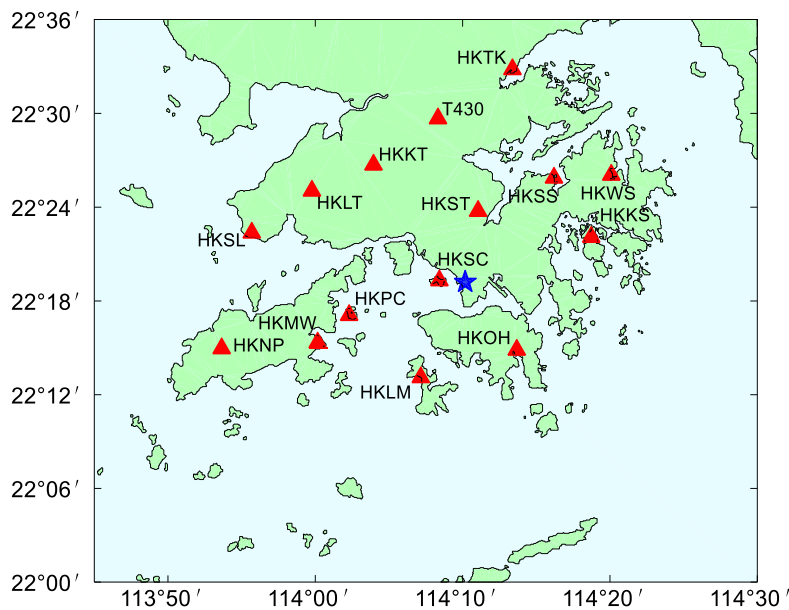
70 **2. Research Area and Data Analysis**

71 *2.1. Study Area*

72 The study area is between 113.75°E-114.5°E and 22°N-22.6°N as shown in Figure 1. There are 15 continues
73 GNSS stations belonging to the Hong Kong SatRef Network deployed in the study area. They are all equipped
74 with Leica GNSS receivers and antennas to receive the GNSS signals and automatic meteorological devices



75 to record the temperature, pressure, and relative humidity. The average inter-distance between stations is about
76 10 km. The altitudes of the highest station (HKNP) and the lowest station (HKLM) are 354 m and 10 m.
77 Therefore, this network is vertically flat.



78
79 **Figure 1.** Research area of the experiment. The red triangles indicate the GNSS stations and the blue star
80 indicates the radiosonde station in Hong Kong.

81 2.2. Data Analysis

82 Two periods of GNSS observation data are processed to generate ZTD and Slant Wet Delay (SWD). One is a
83 rainy period from July 20 to 26, 2015 when Hong Kong suffered the heaviest daily rainfall of 2015 (191.3
84 mm rainfall on July 22). The other is a rainless period from August 1 to 7, 2015.

85 We adopt the same settings as detailed in Zhang et al. (2017) to process the GNSS data. The precise point
86 positioning module in Bernese 5.0 software is used to process the GNSS observations and generate GNSS
87 ZTD data. The International GNSS Service final orbit and clock products are used. The differential code
88 Biases (DCB) is corrected by products from the Center for Orbit Determination in Europe. Antenna phase
89 center offsets and variations, phase wind-up, Earth tides, Earth rotation, ocean tides and relativistic effects are
90 corrected by conventional methods detailed in (Kouba and Héroux, 2001). We use the ionosphere-free
91 combination of double frequencies to eliminate the first order ionospheric delay and the higher-order terms
92 are ignored. The tropospheric delay models are Saastamoinen model (Saastamoinen, 1972) and Neill mapping
93 functions (Niell, 1996). The zenith hydrostatic delay is estimated and removed from the ZTD by using the in-
94 situ pressure observations and Saastamoinen model. The cut-off elevation angle is 10°. The SWD is
95 reconstructed by mapping the ZWD and horizontal gradients onto the ray direction. The phase residuals are
96 added to SWD to consider the inhomogeneity of the troposphere.

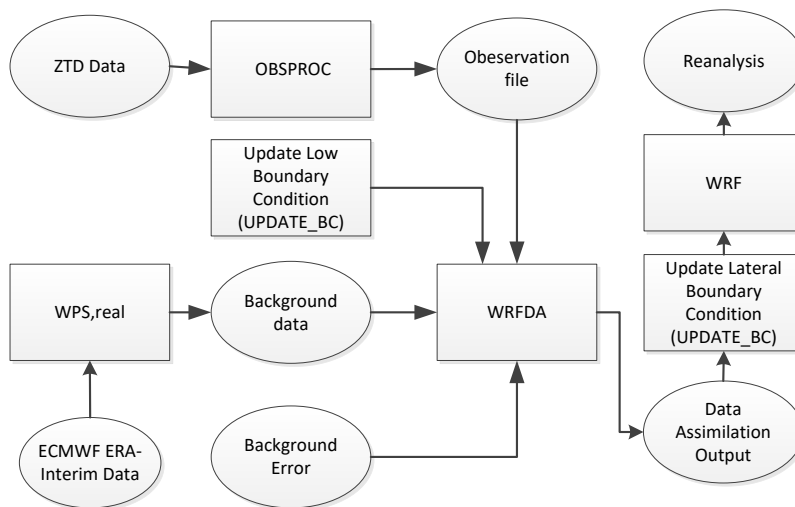
97 3. Method



98 *3.1. WRF model and Data assimilation*

99 The WRF model version 3.7 is used in this study. The WRFDA-3DVAR is used to assimilate the GNSS ZTD
 100 to improve the background data. The WRFDA is designed to obtain the best estimate of the actual atmospheric
 101 state at any analysis time (Barker et al., 2004; Huang et al., 2008; Barker et al., 2012; Singh et al., 2017). In
 102 this study, the WRFDA estimates the atmosphere state that best fits the ZTD observations. We use the
 103 following settings to run the WRFDA and WRF models. The horizontal resolution is set to 3 km. The
 104 atmosphere is vertically divided into 45 layers. The pressure of the top layer is 50 hpa. The physics options in
 105 this study are unified Noah land-surface model (Tewari et al., 2004), Revised MM5 Monin-Obukhov scheme
 106 (Monin and Obukhov, 1954), and Yonsei University planetary boundary layer scheme (Hong et al., 2006).
 107 The Rapid Radiative Transfer Model (Mlawer et al., 1997) and Dudhia's scheme (Dudhia, 1989) were used
 108 for longwave radiation and shortwave radiation, respectively. The nested mode is not used.

109 We use the reanalysis data from European Center for Medium-Range Weather Forecasts (ECMWF) ERA-
 110 Interim as the background data, whose nominal spatial resolution is $0.125^\circ \times 0.125^\circ$. The procedures to do the
 111 assimilation experiments are shown in Figure 2.



112

113 **Figure 2.** Flowchart of data assimilation using the WRF model.

114 The background data are processed by WRF preprocessing system (WPS). The WRFDA is run with the
 115 generic CV3 option, and the default background error is adopted in this study. The GNSS ZTDs are the input
 116 observations for WRFDA. We run WRFDA and obtain the output which is then used to initialize the WRF
 117 model. For comparison's sake, we also run the WRF model using the WPS output as the initial conditions.

118 When we obtain the reanalysis from the WRF model, we use Equation (1) to calculate WR (Vedel and
 119 Huang, 2004).

$$WR = \frac{P}{T} \times \left(k_1 + \frac{k_2}{T} \right) \quad (1)$$



120 where P_w is the water vapor pressure in Pascal, T is the temperature in Kelvin. $k_1=2.21\times 10^{-7}$,
121 $k_2 = 3.73\times 10^{-3}$. Equation (2) is used to calculate P_w from reanalysis data.

$$P_w = \frac{P \times q}{0.622} \quad (2)$$

122 where P is the pressure in Pascal, q is the specific humidity in kg/kg.

123 3.2. GNSS tomography

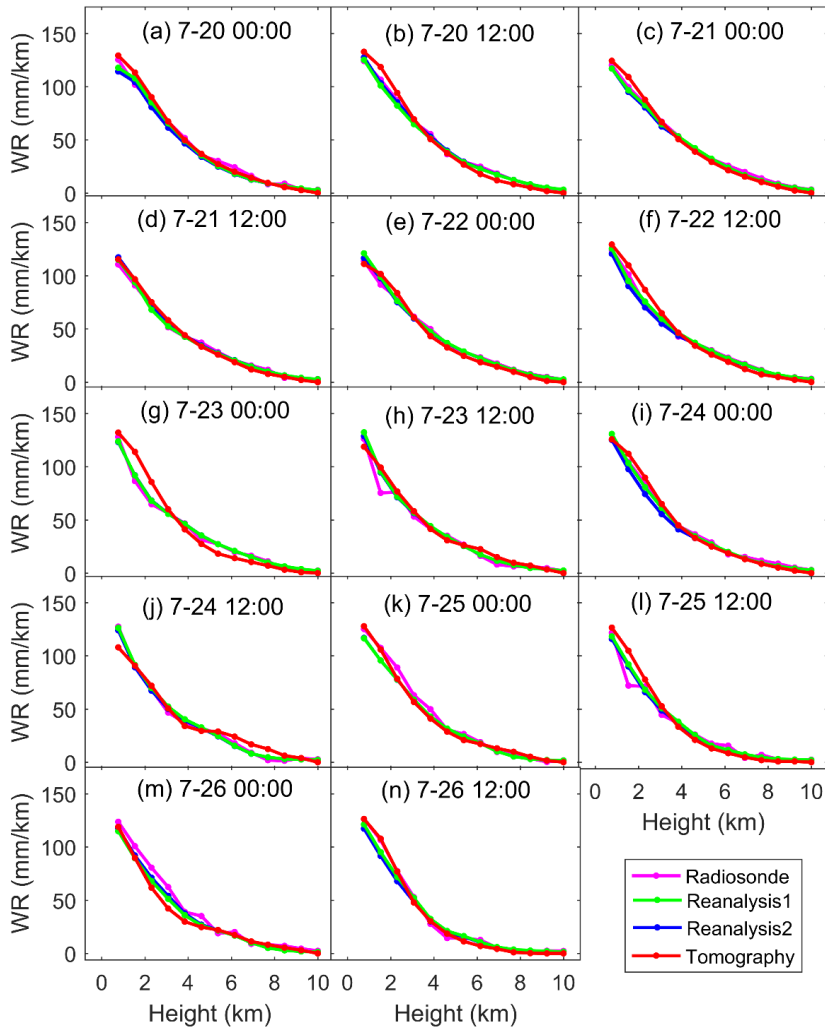
124 The limited number of stations, flat vertical distribution of stations, and bad satellite-station geometry impose
125 serious ill-posed problem in the GNSS WR tomography. To well handle this problem, we use the tomography
126 method proposed by Zhang et al. (2017). This method is based on the adaptive Laplacian smoothing and
127 Helmert Variance Component Estimation. It also uses the meteorological data from each GNSS station to
128 constrain the WR near the ground. This tomography strategy is free of a priori information, which makes it an
129 independent technique and thus ensures the fairness when the tomography technique is compared with the
130 WRF model. The WR can be retrieved directly by this tomography strategy when the SWDs are used as
131 observations. The troposphere is vertically divided into 13 layers with a constant thickness of 800 meters, and
132 horizontally divided into grids whose resolution is ~10 km in longitudinal direction and ~8 km in latitudinal
133 direction.

134 4. Results

135 The radiosonde data are used to validate the WR derived from GNSS tomography and reanalysis. Since the
136 radiosonde launches at 0:00 and 12:00 UTC daily, the WR at these time points are validated. Equation (1) is
137 also used to calculate WR from radiosonde data. In the horizontal direction, we use WR from reanalysis at the
138 nearest four grids to interpolate the WR at the radiosonde location by the bilinear interpolation method. In the
139 vertical direction, we interpolate the above results and the radiosonde observation to the centers of the
140 associated tomography voxels by the linear interpolation method. Finally, the WR from reanalysis and GNSS
141 tomography are validated by the radiosonde data. For simplicity, WR from radiosonde data, reanalysis that
142 assimilate ZTD, reanalysis that without assimilating GNSS ZTD, and GNSS tomography are denoted as
143 “Radiosonde”, “Reanalysis1”, “Reanalysis2”, and “Tomography” hereinafter.

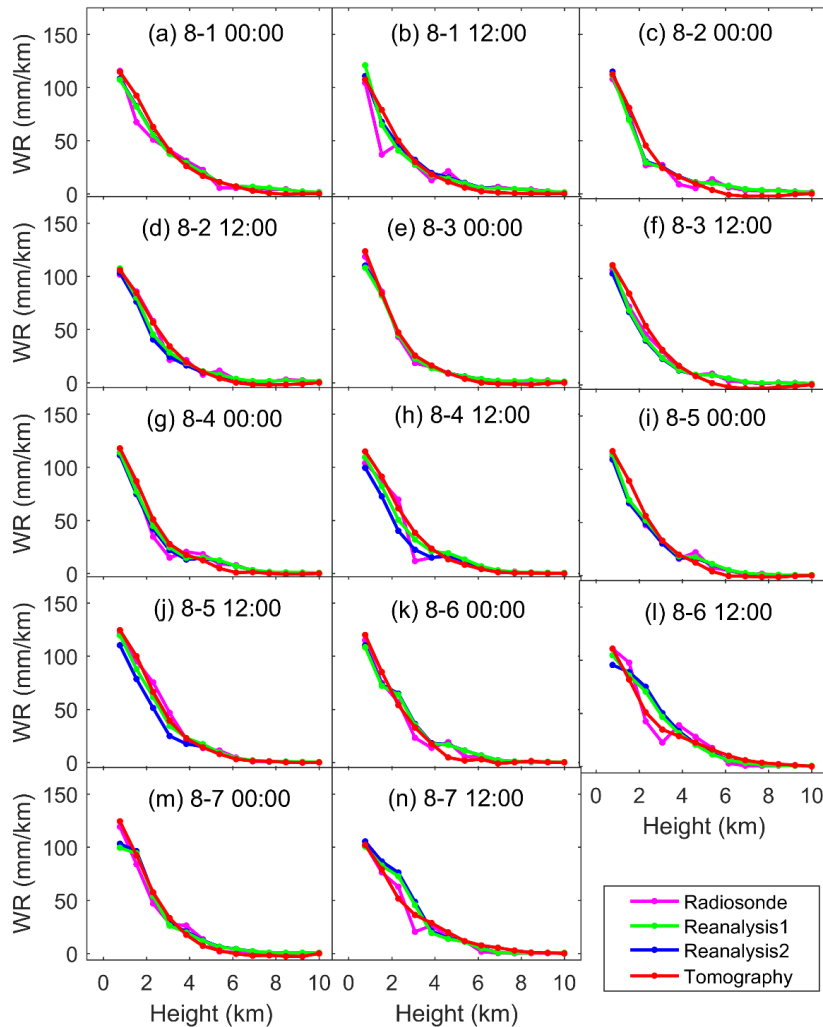
144 Figures 3 and 4 show the vertical profiles of the Reanalysis1, the Reanalysis2, the Tomography, and the
145 Radiosonde in the July and August periods, respectively. The Reanalysis1, Reanalysis2, and Tomography
146 agree well with the Radiosonde, which indicates that these three methods successfully retrieved the vertical
147 profile of the WR. It is also observed that the Reanalysis1, the Reanalysis2, and the Tomography agree better
148 with the Radiosonde in the July period than in the August period. This difference should be due to the vertical
149 distribution of WR. Though Hong Kong suffered heavy rain in the July period, the WR was more evenly
150 distributed from 0 to 10 km height than that in the August period. In the rainless August period, the WR was
151 highly concentrated in the lower troposphere (< 6 km) and its vertical changes were very sharp. This situation
152 decreased the performance of the tomography technique and the WRF model. This may also indicate that both
153 methods have decreased capabilities in retrieving WR in highly changing troposphere. Compared with
154 Reanalysis2, the Reanalysis1 is slightly improved, but the improvement is not significant. The difference

155 between the Tomography and the Reanalysis1 is obvious at some time points in the rainless period (e.g., 12:00
156 on August 4 and 5).



157

158 **Figure 3.** Comparisons among WR derived from reanalysis, tomography, and radiosonde in the rainy
159 period, 2015.

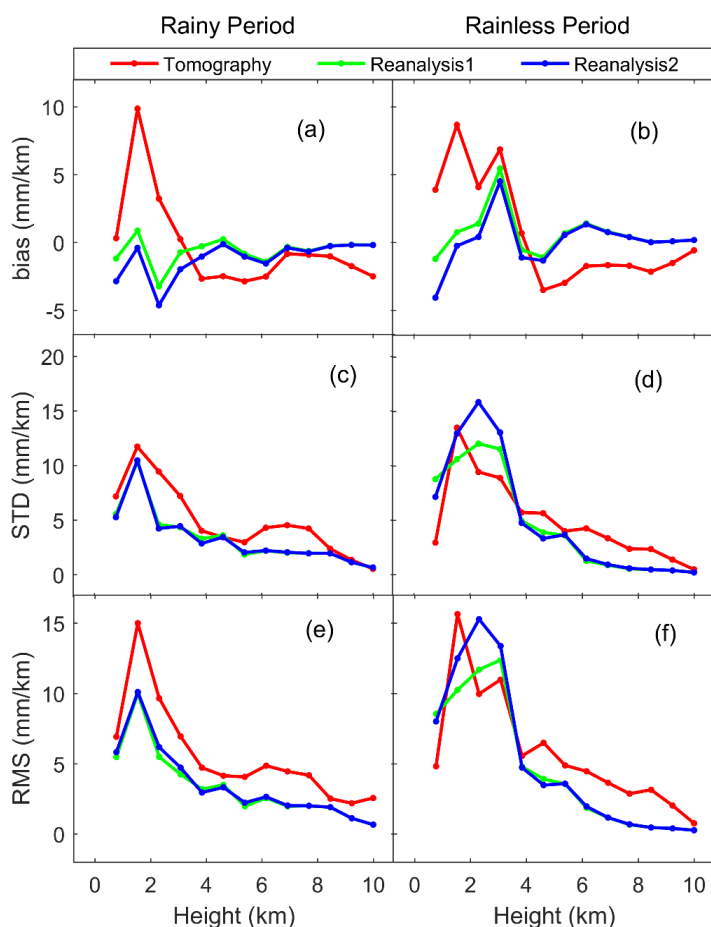


160

161 **Figure 4.** Comparisons among WR derived from reanalysis, tomography, and radiosonde in the rainless
 162 period, 2015.

163 Figure 5 shows the statistics of the bias, standard deviation (STD), and Root Mean Square (RMS) of the
 164 Tomography, the Reanalysis1, and the Reanalysis2 validated by the Radiosonde at different heights. In the
 165 rainy period, bias of Reanalysis1 is smaller than that of Reanalysis2, but the differences are not obvious in
 166 terms of STD and RMS. In the rainless period, the bias of Reanalysis1 in the lower troposphere is slightly
 167 greater than that of the Reanalysis2. Overall, the differences between Reanalysis1 and Reanalysis2 are not
 168 significant.

169 In the rainy period, the bias, STD, and RMS of the Tomography are greater than that of the Reanalysis1
 170 in most of the time. But in the rainless period, the STD and RMS of the Tomography tend to be smaller than
 171 that of the Reanalysis1 in the lower troposphere, but its bias is still greater. In general, the WRF model
 172 performs better than the tomography technique in most of the cases, but in the lower troposphere in the rainless
 173 period the tomography may perform better than the WRF model.



174

175 **Figure 5.** Statistics of bias, STD, and RMS of Tomography, Reanalysis1, and Reanalysis2 validated by
 176 the Radiosonde.

177 Table 1 shows the bias, STD, and RMS of Tomography, Reanalysis1, and Reanalysis2 validated by the
 178 Radiosonde. In the whole troposphere in the rainy period, Tomography has the smallest bias but the largest
 179 STD and RMS. The Reanalysis1 and Reanalysis2 have the similar STD and RMS that are much smaller than
 180 that of the Tomography. But the Reanalysis2 has the largest bias than Reanalysis1 and the Tomography. In
 181 the lower troposphere in the rainy period, Reanalysis1 has the smallest STD and RMS while the Tomography
 182 has the largest ones. The bias of Tomography is positive in the low troposphere but negative in the upper
 183 troposphere, this should be due to the vertical smoothing constraints imposed on the WR. In the upper
 184 troposphere in the rainy period, Tomography has the largest bias, STD, and RMS while Reanalysis1 has the
 185 smallest ones. Overall, both the tomography and the reanalysis results have larger bias, STD, and RMS in the
 186 lower troposphere than in the upper troposphere, indicating both the tomography technique and the WRF
 187 model has decreased capabilities in the lower troposphere.

188 In the whole troposphere in the rainless period, Reanalysis2 has the smallest bias but the largest
 189 RMS. The STD and RMS of Tomography are larger than Reanalysis1. In the lower troposphere in the rainless
 190 period, Reanalysis2 has the largest RMS and STD while Reanalysis1 has the smallest ones. In the low



191 troposphere in the rainless period, the performance of Tomography is not as good as Reanalysis1 in terms of
 192 RMS. However, in the upper troposphere in the rainless period, the Tomography has relatively larger bias,
 193 STD and RMS than the reanalysis results.

194 **Table 1.** Statistics of bias, RMS and STD of Tomography, Reanalysis validated by the radiosonde WR.
 195 Unit is mm/km.

		Rainy Period			Rainless Period		
		bias	STD	RMS	bias	STD	RMS
	Reanalysis1	-0.64	4.11	4.15	0.63	6.34	6.35
Total	Reanalysis2	-1.19	4.15	4.31	0.10	7.28	7.26
	Tomography	-0.31	6.51	6.50	0.63	7.01	7.02
Low	Reanalysis1	-0.74	5.37	5.40	0.77	8.62	8.61
(< 5.6 km)	Reanalysis2	-1.73	5.37	5.62	-0.19	9.90	9.85
	Tomography	0.80	8.20	8.19	2.52	8.83	9.13
Upper	Reanalysis1	-0.51	1.75	1.81	0.47	0.86	0.97
(≥ 5.6 km)	Reanalysis2	-0.55	1.77	1.84	0.45	0.91	1.01
	Tomography	-1.60	3.26	3.62	-1.57	2.63	3.05

196 In general, assimilating GNSS ZTD into the WRF model could slightly improve the WR but the
 197 improvement is not significant. The reanalysis WR overall outperforms the tomography WR but the
 198 tomography WR may be better in the lower troposphere in the rainless period. The results are better in the
 199 rainy period than in the rainless period, which is mainly due to the sharp vertical variation of WR in the rainless
 200 period.

201 5. Discussion

202 In the rainless period, due to the sharp vertical variations of WR, the Tomography, the Reanalysis have
 203 decreased performance in retrieving the WR, especially in the lower troposphere. Compared with the results
 204 in the rainy period, the RMS of the Tomography and the Reanalysis1 increases by 0.94 mm/km, 3.24 mm/km
 205 in the rainless period, respectively. The accuracy decrease is more significant in the Reanalysis1 than in the
 206 Tomography, resulting in that the tomographic WR becomes better than the reanalysis WR (Figures 5d and
 207 5f) in the low troposphere.

208 When assimilating ZTD into the WRFDA, we only use the total column water vapor and do not know its
 209 vertical structure. This leads to that the assimilation of ZTD has limited improvement in retrieving the vertical
 210 structure of the WR. Therefore, it is natural to consider assimilating good tomographic WR into the WRFDA
 211 model to improve the retrieval of the vertical structure of WR. At present, WRFDA could not assimilate WR

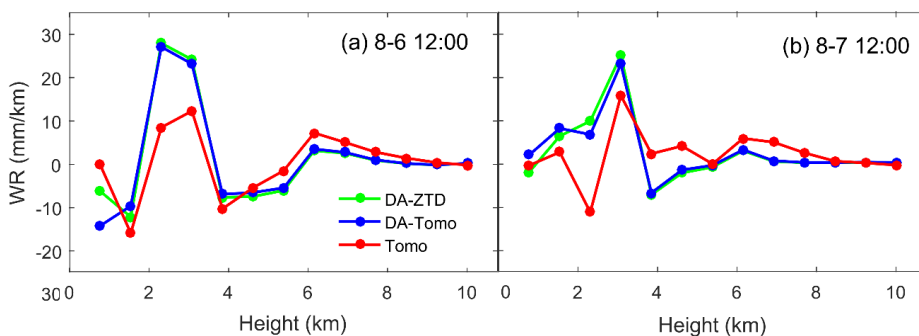
212 directly, but can assimilate meteorological parameters such as relative humidity, temperature and pressure. To
 213 assimilate the tomographic WR, we convert WR to relative humidity.

214 The relationship between relative humidity (RH) and P_w is shown as Equation (3).

$$RH = \frac{P_w}{P_s} \quad (3)$$

215 where P_s is the saturated water vapor pressure which is related to temperature and can be calculated by Wexler
 216 formula (Wexler, 1976, 1977). The P_w is calculated by Equation (1). The needed temperature and pressure
 217 data are from the reanalysis data. After converting the tomographic WR to RH , we assimilate the RH together
 218 with the corresponding temperature and pressure to the WRFDA. Then, the similar procedures as described
 219 in Section 3.1 are performed to generate reanalysis.

220 The Tomography agrees better with the Radiosonde than the Reanalysis1 and Reanalysis2 in the lower
 221 troposphere below 3 km at 12:00 on August 6 (Figure 4l) and at 12:00 on August 7 (Figure 4n). So, we
 222 assimilate the tomographic WR below 3 km into the WRFDA model at these two time points. The generated
 223 reanalysis data are denoted as “Reanalysis3”. The difference between Reanalysis3 and Radiosonde is denoted as
 224 as “DA-Tomo”. The difference between Reanalysis1 and Radiosonde is denoted as “DA-ZTD”. The
 225 difference between Tomography and Radiosonde is denoted as “Tomo”. The differences at different heights
 226 at 12:00 on August 6 and 7 are shown in Figure 6.



227

228 **Figure 6.** Differences between WR obtained by various methods and radiosonde WR.

229 Figure 6 shows that the DA-ZTD is very close to the DA-Tomo. The average DA-ZTD is 6.04 mm/km
 230 and the average DA-Tomo is 5.92 mm/km. This indicates that assimilating tomographic WR into the WRF
 231 model can slightly improve the WR retrieve. The large uncertainty (8.35 mm/km) of the tomography WR in
 232 the lower troposphere may limit the improvement.

233 6. Conclusions

234 GNSS WR tomography and data assimilation experiments are conducted in Hong Kong during a rainy and a
 235 rainless period to test the capabilities of the tomography technique and the WRF model in retrieving WR. The
 236 results show that both the tomography technique and the WRF model can retrieve WR that agrees well with
 237 the radiosonde data.



238 In the rainy period in the whole troposphere, the RMS of Tomography, Reanalysis1 and Reanalysis2
239 6.50 mm/km, 4.31 mm/km, and 4.15 mm/km. The RMS becomes 7.02 mm/km, 6.35 mm/km, and 7.26 mm/km
240 in the rainless period. Both methods obtained better WR in the rainy period than in the rainless period. We
241 infer that the sharp vertical variations of WR reduced the WR retrieving accuracy in the rainless period. In
242 most of the cases, the reanalysis WR outperforms the tomographic WR but the tomographic WR may be better
243 than the reanalysis WR in the lower troposphere in the rainless period. By assimilating better tomographic
244 WR in the lower troposphere into the WRFDA model, we slightly improve the reanalysis WR.

245 The above results suggest that both the WRF model and the tomography technique can retrieve good WR
246 but also have drawbacks. If we combine the two by assimilating good tomographic WR into the WRFDA, we
247 may further improve the performance of the WRF model in retrieving the water vapor field.

248

249 *Data availability.* All the data used in this paper are available upon request by email (sggzb@whu.edu.cn).

250

251 *Conflicts of Interest.* The authors declare no conflict of interest.

252

253 *Acknowledgments.* The authors would like to thank the Survey and Mapping Office/Lands Department of
254 Hong Kong, IGRA, and ECMWF for providing experimental data, and thank Mesoscale and Microscale
255 Meteorology Laboratory of the National Center for Atmospheric Research for providing WRF model. This
256 research is funded by the National Science Foundation of China (41704004; 41574028) and supported by Key
257 Laboratory of Geospace Environment and Geodesy, Ministry of Education, Wuhan University (17-02-03).

258

259 **References**

260 Adams, K.; Fernandes, S.; Maia, F. GNSS Precipitable Water Vapor from an Amazonian Rain Forest Flux
261 Tower. *Journal of Atmospheric & Oceanic Technology*, 28(10):1192-1198, doi: 10.1175/jtech-d-11-00082.1,
262 2011.

263 Altshuler E E. Tropospheric range-error corrections for the Global Positioning System. *IEEE Transactions on*
264 *Antennas & Propagation*, 46(5):643-649, doi: 10.1109/8.668906, 2002.

265 Altuntac, E. Quasi-Newton Approach for an Atmospheric Tomography Problem. eprint arXiv:1511.08022,
266 Available at: <https://arxiv.org/pdf/1511.08022.pdf> (accessed on 4 May 2018) , 2015.

267 Askne, J.; Nordius, H. Estimation of Tropospheric Delay for Microwaves from Surface Weather Data. *Radio*
268 *Sci.*, 22(3): 379-386, doi: 10.1029/rs022i003p00379, 1987.

269 Barker, D.; Huang, Y.; Liu, Z.; Auligné, T.; Zhang, X.; Rugg, S.; Demirtas, M. The weather research and
270 forecasting model's community variational/ensemble data assimilation system: WRFDA. *Bulletin of the*
271 *American Meteorological Society*, 93(6), 831-843, doi: 10.1175/BAMS-D-11-00167.1, 2012.



- 272 Barker, M.; Huang, W.; Guo, R.; Bourgeois, J.; Xiao, N. A three-dimensional variational data assimilation
273 system for MM5: Implementation and initial results. *Monthly Weather Review*, 132(4), 897-914, doi:
274 10.1175/1520-0493(2004)132<0897:ATVDAS>2.0.CO;2, 2004.
- 275 Bender, M.; Dick, G.; Ge, M.; Deng, Z.; Wickert, J.; Kahle, G.; Tetzlaff, G. Development of a GNSS water
276 vapour tomography system using algebraic reconstruction techniques. *Advances in Space Research*, 47(10):
277 1704-1720, doi: 10.1016/j.asr.2010.05.034, 2011.
- 278 Bennitt, V.; Jupp, A. Operational assimilation of GPS zenith total delay observations into the Met Office
279 numerical weather prediction models. *Monthly Weather Review*, 140(8), 2706-2719, doi:10.1175/MWR-D-
280 11-00156.1, 2012.
- 281 Bevis, M.; Businger, S.; Herring, A.; Rocken, C.; Anthes, A.; Ware, H. GPS meteorology: remote sensing of
282 atmospheric water vapor using the global positioning system. *J. Geophys. Res.*, 97(D14): 15,787-15,801, doi:
283 10.1029/92JD01517, 1992.
- 284 Bokoye, I.; Royer, A.; O'Neill, T.; Cliche, P.; McArthur, B.; Teillet, M.; Thériault, M.. Multisensor analysis
285 of integrated atmospheric water vapor over Canada and Alaska. *J. Geophys. Res.*, 108(D15): 4480, doi:
286 10.1029/2002jd002721, 2003.
- 287 Boniface, K.; Ducrocq, V.; Jaubert, G.; Yan, X.; Brousseau, P.; Masson, F.; Doerflinger, E. Impact of high-
288 resolution data assimilation of GPS zenith delay on Mediterranean heavy rainfall forecasting. *Annales*
289 *Geophysicae*, 27: 2739-2753, doi:10.5194/angeo-27-2739-2009, 2009.
- 290 Cao, Y.; Chen, Y.; Pingwha, I. Wet Refractivity Tomography with an improved Kalman-Filter Method.
291 *Advances in Atmospheric Sciences*, 23(5):693-699, doi: 10.5194/angeo-35-87-2017, 2006.
- 292 Carvalhoabc, D. A sensitivity study of the WRF model in wind simulation for an area of high wind energy.
293 *Environmental Modelling & Software*, 33(7):23-34, doi:10.1016/j.envsoft.2012.01.019, 2012.
- 294 Dudhia, J. Numerical Study of Convection Observed during the Winter Monsoon Experiment Using a
295 Mesoscale Two-Dimensional Model. *J.atmos.*, 46(46): 3077-3107, doi: 10.1175/1520-
296 0469(1989)046<3077:nsocod>2.0.co;2, 1989.
- 297 Faccani, C.; Ferretti, R.; Pacione, R.; Paolucci, T.; Vespe, F.; Cucurull, L. Impact of a high density GPS
298 network on the operational forecast. *Advances in Geosciences*, 2, 73-79, doi:10.5194/adgeo-2-73-2005, 2005.
- 299 Flores, A.; De Arellano, G.; Gradinarsky, P.; Rius, A. Tomography of the Lower Troposphere Using a Small
300 Dense Network of GPS Receivers. *IEEE Transactions on Geoscience and Remote Sensing*, 39(2): 439-447,
301 doi: 10.1109/36.905252, 2001.
- 302 Flores, A.; Ruffini, G.; Rius, A. 4D tropospheric tomography using GPS slant wet delays. *Annales*
303 *Geophysicae*, 18(2):223-234, doi: 10.1007/s005850050025, 2000.
- 304 Grejner-Brzezinska, A. GPS-PWV estimation and validation with radiosonde data and numerical weather
305 prediction model in Antarctica. *Gps Solutions*, 17(1):29-39, doi: 10.1007/s10291-012-0258-8, 2013.



- 306 Gutman, I.; Bock, Y. Tropospheric Signal Delay Estimates Derived from Numerical Weather Prediction
307 Models and Their Impact on Real-Time GNSS Positioning Accuracy. AGU Fall Meeting, San Francisco, USA,
308 10-14 December 2007.
- 309 Hirahara, K. Local GPS tropospheric tomography. *Earth Planets & Space*, 52(11):935-939, doi:
310 10.1186/bf03352308, 2000.
- 311 Hong, Y.; Noh, Y.; Dudhia, J. A New Vertical Diffusion Package with an Explicit Treatment of Entrainment
312 Processes. *Monthly Weather Review*, 134(9):2318, doi: 10.1175/MWR3199.1, 2006.
- 313 Huang, Y.; Xiao, Q.; Barker, M.; Zhang, X.; Michalakes, J.; Huang, W.; Dudhia, J. Four-Dimensional
314 Variational Data Assimilation for WRF: Formulation and Preliminary Results. *Monthly Weather Review*,
315 137(1):299-314, doi:10.1175/2008MWR2577.1, 2008
- 316 Jankov, I.; Gallus Jr.; W. A.; Segal, M.; Shaw, B.; Koch, E. The Impact of Different WRF Model Physical
317 Parameterizations and Their Interactions on Warm Season MCS Rainfall. *Weather & Forecasting*, 20(6):1048-
318 1060, doi:10.1175/WAF888.1, 2005.
- 319 Kouba, J.; Héroux, P., Precise point positioning using IGS orbit and clock products. *GPS Solut.* 5, 12-28,
320 doi:10.1007/PL00012883, 2001.
- 321 Lanyi, G. Tropospheric delay effects in radio interferometry. *Telecommunications & Data Acquisition*
322 *Progress Report*, 78,152-159. Available at: http://ipnpr.jpl.nasa.gov/progress_report/42-78/78N.PDF
323 (accessed on 4 May 2018), 1984.
- 324 Li, X.; Dick, G.; Ge, M.; Heise, S.; Wickert, J.; Bender, M. Real-time GPS sensing of atmospheric water vapor:
325 Precise point positioning with orbit, clock, and phase delay corrections. *Geophysical Research Letters*, 41(10):
326 3615-3621, doi: 10.1002/2014jd021486, 2014.
- 327 Li, X.; Zus, F.; Lu, C.; Dick, G.; Ning, T.; Ge, M.; Schuh, H. Retrieving of atmospheric parameters from
328 multi-GNSS in real time: validation with water vapor radiometer and numerical weather model. *Journal of*
329 *Geophysical Research: Atmospheres*, 120(14): 7189-7204, doi: 10.1002/2015jd023454, 2015.
- 330 Lindskog, M.; Ridal, M.; Thorsteinsson, S.; Tong, N. Data assimilation of GNSS Zenith Total Delays from a
331 Nordic processing centre. *Atmospheric Chemistry & Physics*, 17(22):1-22, doi: 10.5194/acp-2017-567, 2017.
- 332 Lu, C.; Li, X.; Nilsson, T.; Ning, T.; Heinkelmann, R.; Ge, M.; Schuh, H.. Real-time retrieval of precipitable
333 water vapor from GPS and BeiDou observations. *Journal of Geodesy*, 89(9), 843-856, doi: 10.1007/s00190-
334 015-0818-0, 2015.
- 335 Mlawer, J.; Taubman, J.; Brown, D.; Iacono, J.; Clough, A. Radiative transfer for inhomogeneous atmospheres:
336 RRTM, a validated correlated-k model for the longwave. *Journal of Geophysical Research Atmospheres*,
337 102(D14):16663-16682, doi: 10.1029/97JD00237, 1997.
- 338 Moeller, G.; Wittmann; C.; Yan, X.; Weber, R. GNSS tomography and assimilation test cases during the 2013
339 Central Europe floods. EGU General Assembly Conference, Vienna, Austria, 17-22 April 2016.
- 340 Monin, S.; Obukhov, M. Basic laws of turbulent mixing in the surface layer of the atmosphere. *Contrib.*
341 *Geophys. Inst. Acad. Sci. USSR.*, 64:1963-1987. Available at:



- 342 https://www.mcnaughty.com/keith/papers/Monin_and_Obukhov_1954.pdf (accessed on 4 May 2018),
343 1954.
- 344 Niell, E. Global mapping functions for the atmosphere delay at radio wavelengths. *J. Geophys. Res.*, 101, doi:
345 3227-3246, 10.1029/95jb03048, 1996.
- 346 Nilsson, T.; Gradinarsky, L. Water vapor tomography using GPS phase observations: simulation results. *IEEE*
347 *Transactions on Geoscience and Remote Sensing*, 44(10): 2927-2941, doi: 10.1109/TGRS.2006.877755, 2006.
- 348 Pacione, R.; Sciarretta, C.; Faccani, C.; Ferretti, R.; Vespe, F. GPS PW assimilation into MM5 with the
349 nudging technique. *Physics & Chemistry of the Earth Part A Solid Earth & Geodesy*, 26(6-8):6-8,
350 doi:10.1016/S1464-1895(01)00088-6, 2001.
- 351 Perler, D.; Geiger, A.; Hurter, F. 4D GPS water vapor tomography: new parameterized approaches. *Journal*
352 *of Geodesy*, 85(8): 539-550, doi: 10.1007/s00190-011-0454-2, 2011.
- 353 Perler, D.; Geiger, A.; Rothacher, M. Determination of the 4D-Tropospheric Water Vapor Distribution by
354 GPS for the Assimilation into Numerical Weather Prediction Models. AGU Fall Meeting, San Francisco ,USA,
355 5-9 December 2011.
- 356 Rocken, C.; Ware, R.; Van Hove, T.; Solheim, F.; Alber, C.; Johnson, J.; Solheim, F.; Alber, C.; Johnson, J.
357 Sensing atmospheric water vapor with the global positioning system. *Geophys. Res. Lett.*, 20, 2631-2634, doi:
358 10.1029/93gl02935, 1993.
- 359 Rohm, W.; Bosy, J. The verification of GNSS tropospheric tomography model in a mountainous area. *Adv.*
360 *Space Res.*, 47, 1721-1730, doi: 10.1016/j.asr.2010.04.017, 2011.
- 361 Saastamoinen, J. Atmospheric correction for the troposphere and stratosphere in radio ranging of satellites.
362 *Use Artif. Satell. Geod.*, 15, 247-251, doi: 10.1029/GM015p0247, 1972.
- 363 Seko, H.; Shimada, S.; Nakamura, H.; Kato, T. Three-dimensional distribution of water vapor estimated from
364 tropospheric delay of GPS data in a mesoscale precipitation system of the Baiu front. *Earth Planets & Space*,
365 52(11):927-933, doi: 10.1186/bf03352307, 2000.
- 366 Shoji, Y.; Sato, K.; Yabuki, M.; Tsuda, T. PWV Retrieval over the ocean using shipborne GNSS receivers
367 with MADOCA real-time orbits. *SOLA*, 12: 265-271, doi: 10.2151/sola.2016-052, 2016.
- 368 Singh, S.; Mandal, M.; Bhaskaran, K. Impact of radiance data assimilation on the prediction performance of
369 cyclonic storm SIDR using WRF-3DVAR modelling system. *Meteorology & Atmospheric Physics*. (2):1-18,
370 doi:10.1007/s00703-017-0552-7, 2017.
- 371 Tewari, M.; Chen, F.; Wang, W.; Dudhia, J.; LeMone, A.; Mitchell, K.; Cuenca, H. Implementation and
372 verification of the unified noah land surface model in the WRF model. In *Bulletin of the American*
373 *Meteorological Society.*, 2165-2170, doi:10.1007/s11269-013-0452-7, 2004.
- 374 Tregoning, P.; Boers, R.; O'Brien, D.; Hendy, M. Accuracy of absolute precipitable water vapor estimates from
375 GPS observations. *Journal of Geophysical Research: Atmospheres*, 103(D22): 28701-28710, doi:
376 10.1029/98JD02516, 1998.



- 377 Vedel, H.; Huang, X. Impact of ground based GPS data on NWP forecasts. *Journal of the Meteorological*
378 *Society of Japan*, 82, 459-472, doi: 10.2151/jmsj.2004.459, 2004.
- 379 Wang, X.; Wang, X.; Dai, Z.; Ke, F.; Cao, Y.; Wang, F.; Song, L. Tropospheric wet refractivity tomography
380 based on the BeiDou satellite system. *Advances in Atmospheric Sciences*, 31(2), 355-362, doi:
381 10.1109/TGRS.2006.877755, 2014.
- 382 Wang, X., Dai, Z., Zhang, E., Fuyang, K. E., Cao, Y., Song, L.; Lianchun, S. Tropospheric wet refractivity
383 tomography using multiplicative algebraic reconstruction technique. *Advances in Space Research*, 53(1), 156-
384 162, doi: 10.1016/j.asr.2010.04.017, 2014.
- 385 Wexler, A. Vapor Pressure Formulation for Ice. *Journal of Research of the National Institute of Standards-A.*
386 *Physics and Chemistry*, 81A(1): 5-20, doi: 10.6028/jres.081A.003, 1977.
- 387 Wexler, A. Vapor Pressure Formulation for Water in Range 0 to f 00 °C. A Revision. *Journal of Research of*
388 *the national Institute of Standards-A. Physics and Chemistry.*, 80A(5-6): 775-785, doi: 10.6028/jres.080A.071,
389 1976.
- 390 Yao, Y.; Zhang, B.; Xu, C.; Yan, F. Improved one/multi-parameter models that consider seasonal and
391 geographic variations for estimating weighted mean temperature in ground-based GPS meteorology. *Journal*
392 *of Geodesy*, 88(3):273-282, doi: 10.1007/s00190-013-0684-6, 2014.
- 393 Yuan, Y.; Zhang, K.; Rohm, W.; Choy, S.; Norman, R.; Wang, S. Real-time retrieval of precipitable water
394 vapor from GPS precise point positioning. *Journal of Geophysical Research: Atmospheres*, 119(16): 10044-
395 10057, doi: 10.1002/2014jd021486, 2014.
- 396 Zhang, B.; Fan, Q.; Yao, Y.; Li, X. An Improved Tomography Approach Based on Adaptive Smoothing and
397 Ground Meteorological Observations. *Remote Sensing*, 9(9):886, doi: 10.3390/rs9090886, 2017.
- 398 Zhao, Q.; Yao, Y. An improved troposphere tomographic approach considering the signals coming from the
399 side face of the tomographic area. *Annales Geophysicae*, 35(1): 87-95, doi: 10.5194/angeo-35-87-2017, 2017.